


 Cite this: *New J. Chem.*, 2020, 44, 200

# A closer look at the defects and luminescence of nanocrystalline fluorides synthesized *via* ionic liquids: the case of Ce<sup>3+</sup>-doped BaF<sub>2</sub>†

 Rahul Kumar Sharma,<sup>a</sup> Yogendra Nath Chouryal,<sup>a</sup> Anatoly I. Slesarev,<sup>b</sup> Konstantin V. Ivanovskikh,<sup>\*b</sup> Ivan I. Leonidov,<sup>cd</sup> Sandeep Nigam<sup>e</sup> and Pushpal Ghosh<sup>\*a</sup>

Phase pure BaF<sub>2</sub> doped with Ce<sup>3+</sup> (0.1%) nanocrystals are synthesized using an ionic liquid (IL) ([C<sub>4</sub>mim][BF<sub>4</sub>]) assisted solvothermal method where the IL is not only used as a reaction medium and a capping agent, but also as a reaction partner. Subsequently, upon calcining the as-prepared nanocrystals at various temperatures (200, 400, 600 and 800 °C), although the crystal phase remains the same, however, a significant change in the lattice strain and morphology is observed. Tensile strain appears in the nanocrystals calcined at temperatures up to 400 °C, but a reversal of the strain, *i.e.* compressive strain, takes place when calcination is performed at 600 °C and onwards. Nanoflakes are obtained until calcination at 400 °C. However on calcination at 600 °C and beyond, a drastic modification in the morphology is observed. Layer or step-like structures appear due to secondary nucleation of nanoparticles. Meanwhile, the photoluminescence (PL) intensity of Ce<sup>3+</sup> ions gradually decreases with the calcination temperature and finally vanishes at 600 °C/800 °C. To investigate the reasons for the quenching of the PL intensity, thermally stimulated luminescence (TSL) and thermally stimulated exoelectron emission (TSEE) measurements are performed. The TSL and TSEE results indicate that in addition to the domination of deeper electron traps that appear as a high-temperature shift of TSEE glow peaks for both 600 °C and 800 °C, some new types of defects like F vacancies (F-centers) can be present, especially in the 800 °C calcined sample. The conditions leading to the quenching of Ce<sup>3+</sup> luminescence in the nanoparticles are analyzed and discussed.

 Received 2nd September 2019,  
 Accepted 23rd November 2019

DOI: 10.1039/c9nj04526k

[rsc.li/njc](http://rsc.li/njc)

## 1. Introduction

Rare-earth (RE<sup>3+</sup>) ion doped inorganic phosphor nanomaterials are extensively paving the way for numerous applications including photonics, bio-photonics and molecular thermometers.<sup>1–6</sup> In molecular thermometers, it has been revealed that RE<sup>3+</sup> ion doped or RE<sup>3+</sup>-based complexes show temperature dependent variation of the emission intensity (5d–4f).<sup>5</sup> Intraconfigurational, parity-forbidden electronic transitions

between the levels of the 4f configuration, which are highly shielded by high-energy 5s<sup>2</sup> and 5p<sup>6</sup> filled orbitals, are not affected significantly by the external chemical environment. In this way, RE-based phosphor nanomaterials are considered as better candidates for optical applications over semiconductor and organic luminescent nanomaterials.<sup>1–4,6</sup> However, the photodynamic processes and emission intensity of RE<sup>3+</sup> ion doped nanomaterials may extensively depend on numerous factors such as the crystal phase, judicious selection of host materials, the RE<sup>3+</sup> dopant ions, shape, core–shell structure, lattice strain, *etc.*<sup>4</sup> Among them, judicious selection of host materials is a prerequisite for getting good luminescence properties from the nanophosphors. Over the last decade, numerous host materials have been explored for doping with RE<sup>3+</sup> ions.<sup>2,4</sup> Among them, binary and ternary fluorides of group I and II are substantially used for doping with RE ions due to their high refractive index, large band gap, low phonon energy and high thermal and chemical stability.<sup>2,7–9</sup> Furthermore, halides of alkaline earth metals are substantially used as scintillators or X-ray phosphor materials which convert high energy ionizing radiation to visible photons and also have extensive

<sup>a</sup> School of Chemical Sciences and Technology, Department of Chemistry, Dr H. S. Gour University (A Central University), Sagar 470003, Madhya Pradesh, India. E-mail: pushpalghosh27@gmail.com

<sup>b</sup> Institute of Physics and Technology, Ural Federal University, Ekaterinburg 620002, Russia

<sup>c</sup> School of Engineering, Ural Federal University, Ekaterinburg 620002, Russia

<sup>d</sup> Institute of High-Temperature Electrochemistry, UB RAS, Ekaterinburg 620137, Russia

<sup>e</sup> Chemistry Division, Bhabha Atomic Research Centre, Trombay, Mumbai 400085, India

† Electronic supplementary information (ESI) available. See DOI: 10.1039/c9nj04526k

applications in several fields.<sup>10,11</sup> For this purpose, generally single crystal materials are considered as better candidates owing to their high optical qualities.<sup>10,11</sup> It has already been reported that BaF<sub>2</sub> nanoparticles and BaF<sub>2</sub> ceramic materials have shown scintillation properties.<sup>10,12</sup> Quite promising scintillator and radioluminescence properties have been demonstrated for Ce<sup>3+</sup> doped LaF<sub>3</sub>,<sup>13</sup> and mixed Ce<sub>x</sub>La<sub>1-x</sub>F<sub>3</sub> nanocomposites,<sup>14</sup> and Eu<sup>3+</sup> doped LaF<sub>3</sub> nanoparticles.<sup>15</sup>

We point out that scintillator as well as radiation dosimetry materials in the form of nanocrystalline powders are an emerging field of research as the nanoscale induces the appearance of new optical properties. The latter, in turn, bring new conceptions for application of such materials and open opportunities for improvement of the application characteristics of radiation detectors including their sensitivity, spatial and temporal resolution, and radiation hardness. For these reasons, nanosized materials may hold good promise for future applications in new generations of radiation detectors for medical diagnostics, security inspection, radiation monitoring, *etc.*

To design inorganic host materials, several synthesis strategies have been explored to date.<sup>2,4,16–21</sup> An ionic liquid is the combination of organic cations and inorganic/organic anions with a melting point less than 100 °C in ambient conditions.<sup>22–25</sup> Such interesting features of an IL as negligible vapor pressure, large liquidus range, low inflammability and most interestingly its tunability make it superior to traditional molecular solvents.<sup>22–24</sup> By judicious selection of the cation–anion combination, the physical and chemical properties of ILs can be widely tuned. Therefore, they are considered as ‘green and designer’ solvents. Recently, application of ILs has extensively increased in various fields, including electrochemistry, catalysis, energy and nanomaterials design.<sup>16,23–25</sup> Thus, a task specific IL assisted method has become especially popular because it is not only used as a capping agent, but can also be used as a reaction partner (for example as a source of fluoride ions to prepare binary or ternary fluorides) and as a reaction medium.<sup>16–20</sup> For instance, ionic liquids have been utilized as a phase tuning and size and morphology controlling agent of semiconducting and RE-doped nanoparticles.<sup>18,26</sup> In addition, ILs have substantially been used for synthesis of fluoride and phosphate based host materials.<sup>19–21</sup>

In order to evaluate the potential of nanoparticles for application in radiation detector materials such as scintillators, X-ray phosphors or thermoluminescence (TL) dosimeters, the nature of the defects present in the material should be understood. To this end, the thermally stimulated luminescence (TSL) and thermally stimulated exoelectron emission (TSEE) techniques are widely used.<sup>27–32</sup> To create radiation induced defects as well as to populate electron or hole traps related to the defects high energy ionizing radiation (X-rays or gamma rays) is used. This experimental technique has been extensively used to understand the defects in nanomaterials or nanopowder.<sup>32–36</sup> It is well known that defects in the inorganic host nanomaterials have a pivotal impact on the luminescence and thermal properties of RE doped nanomaterials.<sup>37–39</sup>

In this work, we have comprehensively studied the photoluminescence and thermal properties of as-prepared 0.1% Ce<sup>3+</sup>

doped BaF<sub>2</sub> nanoparticles synthesized *via* an ionic liquid ([C<sub>4</sub>mim][BF<sub>4</sub>]) assisted solvothermal method. Herein, the IL is utilized as a reaction partner (a source of fluoride ions), a reaction medium and a templating agent, all ‘three in one’. While calcining the as-prepared nanoparticles in a wide range of temperature (200–800 °C), secondary nucleation controls significant changes in the morphology especially at the higher calcination temperatures. The photoluminescence intensity is observed to decrease at higher temperatures of calcination. It is assumed that drastic morphology changes due to secondary nucleation and defects are playing a major role in the photoluminescence quenching. To get insight into the nature of the defects appearing in the nanoparticles, thermally stimulated luminescence (TSL) and exoelectron emission (TSEE) techniques have been used.

## 2. Materials and methods

### 2.1 Chemicals and preparation of [C<sub>4</sub>mim][Br] and [C<sub>4</sub>mim][BF<sub>4</sub>] ionic liquids

The list of chemicals, their purity and details of the synthesis of the ionic liquids used in this work can be found in the ESI.†

### 2.2 Synthesis of Ce<sup>3+</sup> (0.1%) doped BaF<sub>2</sub> nanoparticles

In a typical reaction, an appropriate amount of barium acetate (0.728 g) was dissolved in ethylene glycol (0.5 ml) with vigorous stirring for 30 minutes. Then an excess amount of [C<sub>4</sub>mim][BF<sub>4</sub>] (4.238 ml) and cerium nitrate hydrate (0.00126 g) was added to the previous mixture. Thereafter, the overall reaction mixture was kept for 5 minutes stirring. Finally, the resultant suspension was transferred into a 100 ml Teflon™ lined autoclave (Parr Instruments, Moline, Illinois, USA) and subsequently heated at 150 °C for 6 hours. As the autoclave was cooled to room temperature naturally, the precipitate was separated by centrifugation, and then washed several times with an ethanol/dichloromethane mixture to obtain a white powder. Finally, the sample was dried at 60 °C for 12 hours in a vacuum oven.

### 2.3 Characterization techniques

Powder X-ray diffraction (PXRD) patterns of the samples were taken with a D8 Advance, BRUKER, equipped with Cu K<sub>α</sub> (1.54060 Å) as the incident radiation. XRD analysis was carried out employing the ICSD-Web database (2019/I). The crystallite size was calculated using the Scherrer equation  $D = K\lambda/\beta \cos \theta$ , where  $K = 0.9$ ,  $D$  represents the crystallite size (Å),  $\lambda$  is the wavelength of Cu-K<sub>α</sub> radiation and  $\beta$  is the corrected half width of the diffraction peak. TEM images of the as-prepared nanoparticles were taken with a Tecnai-STWIN-T30 using a 200 kV electron beam source. Morphology analysis was carried out using a Field Emission Gun Scanning Electron Microscope (NOVA NanoSEM 450). Photoluminescence emission and excitation spectra were measured using a HORIBA JOBIN YVON made Fluoromax-4 spectrofluorometer. TG/DTA measurements were carried out using a Mettler Toledo Thermal Analyzer. The surface areas of the as-prepared and calcined BaF<sub>2</sub> nanoparticles were

investigated using a BET (Brunauer–Emmett–Teller) surface area measurement system (Belsorp MR6, Japan).

The thermally stimulated luminescence (TSL) and thermally stimulated exoelectron emission (TSEE) properties were experimentally studied at Ural Federal University (Russia). The nanopowders for this study were pressed into compact pellets of 4 mm diameter and 1 mm thickness. All the samples were irradiated with an electron beam from a MIRA-2D pulse electron gun with an energy of 150 keV for 15 seconds to get the same radiation dose. TSL and TSEE glow curves were recorded simultaneously with an exoemission spectrometer equipped with a VEU-6 electron multiplier to detect electron exoemission and a MELZ FEU-142 solar-blind photomultiplier sensitive in the spectral range of 112–365 nm to detect the luminescence. The setup allows linear heating of samples in the temperature range of 25–1000 °C with a 0.1–1.0 g rad s<sup>-1</sup> heating rate. The measurements were performed in a vacuum of ~10<sup>-5</sup> Torr.

### 3. Results and discussion

#### 3.1 Structural chemistry

0.1% Ce<sup>3+</sup> doped BaF<sub>2</sub> nanoparticles are prepared using an IL-assisted solvothermal method in which the ([C<sub>4</sub>mim][BF<sub>4</sub>]) IL is used as a reaction medium, a fluoride source and a capping agent, all three in one. The phase purity of the as-prepared nanoparticles is confirmed by using PXRD and all the peaks were found clearly matching those documented in the standard

JCPDS card number C4-452 for BaF<sub>2</sub> (Fig. 1a). Later, by calcining the as-prepared (P1) sample at different temperatures of 200 °C (P2), 400 °C (P3), 600 °C (P4) and 800 °C (P5), no change in the crystal phase of the BaF<sub>2</sub> nanoparticles is observed indicating high thermal stability. The crystallite size of the calcined samples gradually increases with increasing the calcination temperature. The as-prepared (at 60 °C, P1) sample has an average crystallite size of 32.2 nm, while the samples calcined at 200 °C, 400 °C, 600 °C and 800 °C have an average crystallite size of 36.2 nm, 38.5 nm, 71.3 nm and 72.4 nm, respectively. Careful analysis of the cell parameters of the as-prepared and the calcined samples reveals significant changes in the cell parameters too (Table 1).

The lattice strains of the as-prepared (P1) and calcined samples (P2–P5) have been determined using the Williamson–Hall equation (ESI<sup>†</sup>). The result indicates that tensile strain is occurring from the as-prepared nanoparticles (P1) to those calcined at 400 °C (P4). However, the maximum tensile strain is obtained for the as-prepared (at 60 °C, P1) sample ( $\eta = 0.95\%$ ). On the other hand, the samples calcined at higher temperatures reveal the development of compressive strain with strain values of  $-0.298\%$  and  $-0.212\%$  for the samples calcined at 600 °C (P4) and 800 °C (P5), respectively (Fig. 2 and Table 1).

#### 3.2 Thermal properties

It is previously reported that on reducing the size of particles from the bulk to the nanoscale, the melting point is reduced and can be expressed as<sup>40</sup>

$$T_M(D) = T_M(\infty) - \frac{\alpha}{D} \quad (1)$$

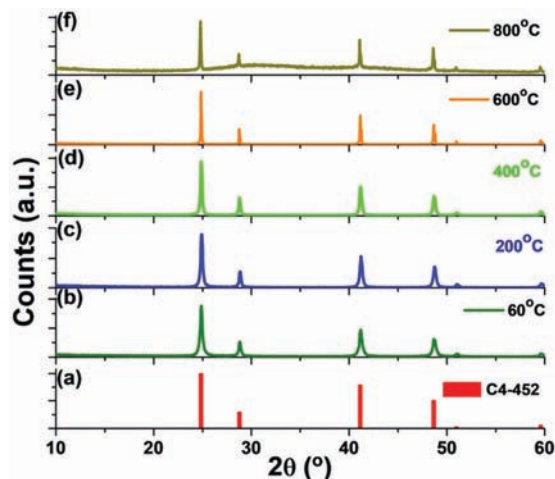


Fig. 1 PXRD patterns of the as-prepared BaF<sub>2</sub>:Ce<sup>3+</sup> (0.1%) nanoparticles and those calcined at different temperatures.

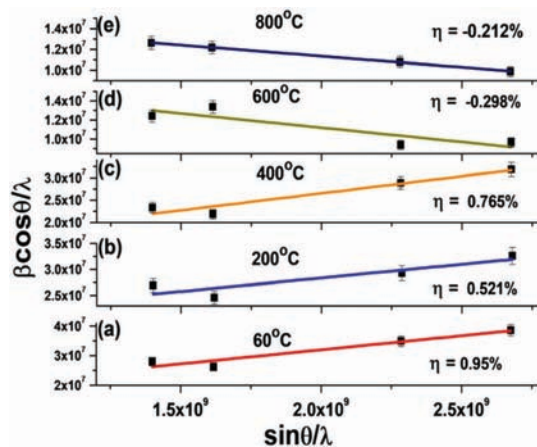


Fig. 2 Lattice strain of BaF<sub>2</sub>:Ce<sup>3+</sup> (0.1%) nanoparticles and those calcined at different temperatures.

Table 1 Phase, crystallite size, cell volume, cell length and average lattice strain of BaF<sub>2</sub>:Ce<sup>3+</sup> (0.1%) nanoparticles synthesized using the [C<sub>4</sub>mim][BF<sub>4</sub>] ionic liquid

Sample ID	Samples	Phase	Crystallite size (111) (nm)	Cell volume (Å <sup>3</sup> )	A (Å)	Average lattice strain (η%)
P1	BaF <sub>2</sub> -Ce (0.1%) (as-prepared, 60 °C)	Cubic	32.2 (±0.3)	238.07(16)	6.197(24)	0.95 (tensile)
P2	BaF <sub>2</sub> -Ce (0.1%) (calcined-200 °C)	Cubic	36.2 (±0.3)	238.13(5)	6.198(7)	0.546 (tensile)
P3	BaF <sub>2</sub> -Ce (0.1%) (calcined-400 °C)	Cubic	38.5 (±0.3)	238.07(7)	6.197(11)	0.765 (tensile)
P4	BaF <sub>2</sub> -Ce (0.1%) (calcined-600 °C)	Cubic	71.3 (±0.3)	238.45(15)	6.201(22)	-0.298 (compressive)
P5	BaF <sub>2</sub> -Ce (0.1%) (calcined-800 °C)	Cubic	72.4 (±0.3)	239.33(9)	6.208(14)	-0.212 (compressive)

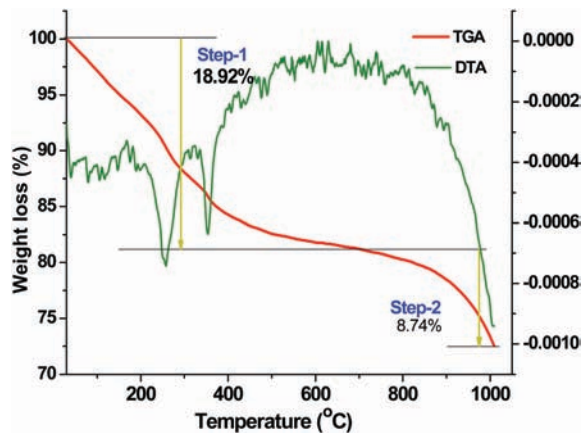


Fig. 3 TGA and DTA curves of the as-prepared  $\text{BaF}_2:\text{Ce}^{3+}$  (0.1%) nanoparticles synthesized using the  $[\text{C}_{4}\text{mim}][\text{BF}_4]$  ionic liquid.

where,  $T_M(D)$  and  $T_M(\infty)$  are the melting points of the particles and bulk particles, respectively;  $\alpha$  is a function of the material (nm K) and  $D$  is the crystallite size of the particles. Dick *et al.* employed the TGA/DTA techniques to illustrate the size dependent change in the melting point of silica coated gold nanoparticles.<sup>41</sup> TGA and DTA curves recorded for the as-prepared  $\text{BaF}_2:\text{Ce}^{3+}$  (0.1%) nanoparticles (P1) are presented in Fig. 3. The TGA data reveal that the weight loss (%) occurs in two steps. The first weight change is found in the temperature range from 30 °C to 650 °C, where the most significant extent of the weight loss (18.92%) is observed. The extent of the weight loss for the temperature range from 650 °C to 1000 °C is found to be smaller (8.74%). The initial weight loss can then be attributed to thermal decomposition of organic compounds such as the precursor or unwashed ionic liquid remaining on the surfaces of the nanoparticles. On the other hand, significant changes are revealed in the DTA result. Particularly, two broad endothermic peaks are observed at 248 °C

and 354 °C with the former about two times broader than the following one.

There is a well established relationship between the size of particles and the width of an endothermic peak, which suggests that the broadening of the endothermic peak is related to the particle size decreasing. Thus, it is likely that the size of the particles responsible for the peak at 248 °C is smaller than that responsible for the peak at 352 °C. Normally, the melting point of bulk  $\text{BaF}_2$  is 1386 °C.<sup>42</sup> In our earlier report, we have noticed a broad endothermic peak at 400 °C for  $\text{BaF}_2:\text{Eu}^{3+}$  nanoparticles and this endothermic event was ascribed to surface melting or full melting.<sup>42</sup> So, in the present case it may be indicated that a melting-like situation arises at 248 °C and 352 °C.

### 3.3 Morphology and local structure

Fig. 4 depicts high magnification FESEM images of the as-prepared (P1) and calcined  $\text{BaF}_2$  nanoparticles (P2–P5). The as-synthesized nanoparticles appear as nanoflakes (Fig. 4a and b). However, at the beginning of calcination, the as-prepared nanoparticles tend to agglomerate, which leads to the formation of larger particles. The edges of the  $\text{BaF}_2$  nanoflakes get thicker and blunt till 400 °C (as shown in Fig. 4c). But a significant change in morphology appears when they are calcined at 600 °C (Fig. 4d and e and Fig. S1a, ESI†). At 600 °C, we observe the formation of larger size particles with big pores that result from merging of the nanoflakes with each other (Fig. 4d and e and Fig. S1a, ESI†). From thermal analysis it is conceived that surface melting or a melting-like situation arises around 354 °C. So nicely connected, bigger size nanoparticles obtained at 600 °C appear first due to melting of nanoparticles which are then re-assembled on cooling (Fig. 4d and e, inset and Fig. S1a, ESI†). This is further supported by zooming, which reveals the surface of bigger particles to be comprised of tiny particles (see Fig. 4e inset and Fig. S1a, ESI†).

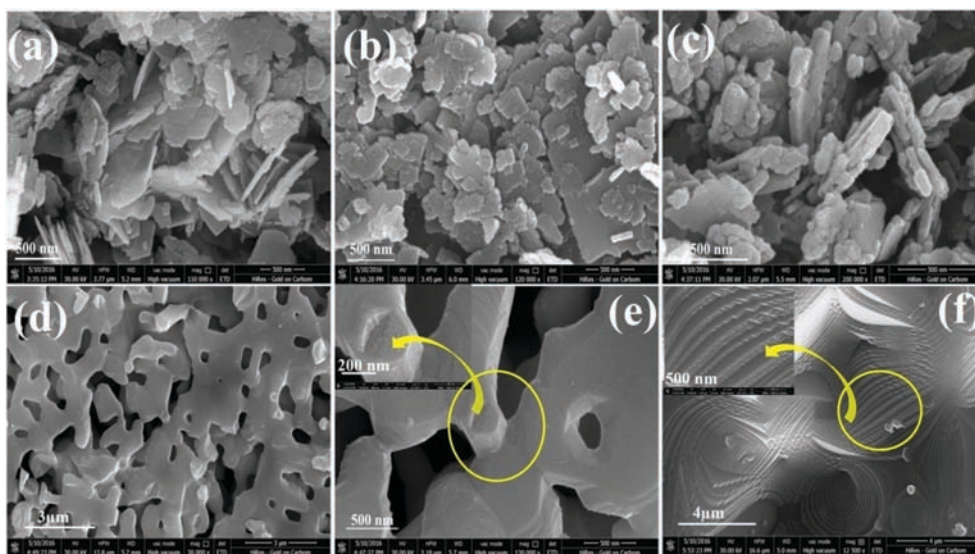


Fig. 4 High magnification FESEM images of (a) as-prepared  $\text{BaF}_2:\text{Ce}^{3+}$  (0.1%) dried at 60 °C, and samples calcined at different temperatures (b) 200 °C, (c) 400 °C, (d) 600 °C, (e) 600 °C, and (f) 800 °C.

This kind of growth is normally associated with the terminology 'secondary nucleation'.<sup>39,42</sup>

The above presented results suggest that calcining the as-prepared nanoparticles at high temperature initially results in surface melting that further leads to smoothing the surface and the formation of a layer-like structure. Again a step/stair-like morphology appears when the samples are calcined at 800 °C (Fig. 4f and Fig. S1b, ESI†). Here the pattern of the step/stair-like shape at 800 °C becomes more regular than that of the calcined sample at 600 °C (P4) while the pores on the surface completely vanish. The latter indicates that at high temperature (800 °C), small particles get further reassembled and subsequently gathered in a layer-by-layer manner while cooling to room temperature. In this way, formation of layer or step/stair-like structures takes place (Fig. 4f and Fig. S1b, ESI†). Fig. 5 and Fig. S2 (ESI†) illustrate the TEM and HRTEM images of the as-prepared (60 °C) (P1) and calcined nanoparticles at 400 °C (P3), 600 °C (P4) and 800 °C (P5) respectively. The TEM images demonstrate that the as-prepared nanoparticles are square/rectangular disc shaped and are highly agglomerated. The nanoparticles which have undergone calcining at a temperature of 400 °C demonstrate blunt and smoother edges of the square/rectangular discs compared to the as-prepared sample (Fig. 5c and d). Such kinds of changes have been already observed in the highly magnified FESEM images of the same sample (400 °C calcined sample, P3). Meanwhile, the morphology is shown to drastically transform from square/rectangular disc-shape to highly agglomerated irregular spherical shape on calcining at 600 °C. The irregular spherical shape particles reveal agglomeration, which gives rise to the formation of the bigger size particles. The 800 °C calcined sample is also

comprised of some amount of small, non-uniform spherical shape particles which are highly agglomerated to form bigger size particles. These results evidently confirm the transformation of the morphology from square/rectangular shape nanoparticles to a layer-like structure depending on the calcination temperature, which can be clearly seen from the FESEM images (Fig. 4 and Fig. S1, ESI†). To depict the growth of the particles in the nanoscale regime, we have performed a comprehensive study of high-resolution TEM (HRTEM) images.

It was revealed that the growth of the nanoparticles takes place along the predominant (111) plane. In addition to the (111) plane, the (200) plane also contributes to the growth of the particles calcined at 400 °C. Whilst the samples calcined at 600 °C (P4) and 800 °C (P5) predominately grow along the (111) plane, the 800 °C calcined sample (P5) demonstrates the presence of substantial point defects. We relate the latter to missing atoms from the array of the planes, which are marked by a rectangular box and circles in Fig. S2 (ESI†). The composition and distribution of ions in the as-prepared 0.1% Ce-doped BaF<sub>2</sub> nanoparticles are confirmed through EDX and elemental mapping (Fig. S3 and S4, ESI†). A considerable change in surface area upon calcination is noticed.

To further confirm the presence of a calcination temperature-dependent change in the morphology of the samples, we have performed BET surface area analysis. The as-prepared sample shows a relatively high surface area (25.29 m<sup>2</sup> g<sup>-1</sup>). Upon calcining the samples, the surface area demonstrates a well pronounced decrease. For example, for the 200 and 400 °C calcined samples the surface areas are found to be 14.45 m<sup>2</sup> g<sup>-1</sup> and 10.22 m<sup>2</sup> g<sup>-1</sup> respectively. However, a significant decrease in the specific surface area is noticed for the 600 °C (1.54 m<sup>2</sup> g<sup>-1</sup>) sample, confirming coalescence of nanoparticles after a certain annealing temperature.

### 3.4 Luminescence properties

Fig. 6 shows the photoluminescence excitation and emission spectra of the as-prepared (P1) and calcined at different temperatures (P2–P5) BaF<sub>2</sub>:Ce<sup>3+</sup> (0.1%) nanoparticles. The emission spectra of P1, P2 and P3 nanoparticles present an emission band centered near 352 nm. The band is best resolved in the case of the as-prepared nanoparticle (P1) sample with local peaks located at 330 and 355 nm, which correspond to electric-dipole transitions from the lowest 5d(<sup>2</sup>E<sub>g</sub>) level to spin-orbit coupled 4f(<sup>2</sup>F<sub>J</sub>) states.<sup>43</sup> The excitation spectrum recorded monitoring the maximum of the emission band at 352 nm is dominated by a broad excitation band centered near 290 nm, which is assigned to the electronic transition from the ground state 4f(<sup>2</sup>F<sub>5/2</sub>) to the doublet <sup>2</sup>E(<sub>g</sub>) state (unresolved) of the excited 5d state.

As long as the samples are measured in nearly the same conditions, their spectra can be confronted and compared. Comparing the emission spectra of the samples shows that the highest intensity of the Ce<sup>3+</sup> 5d–4f emission peak is observed for the as-prepared (60 °C calcined, P1) sample.

The emission peak intensity drops to less than half of its initial value for the 400 °C calcined sample (P3) and vanishes

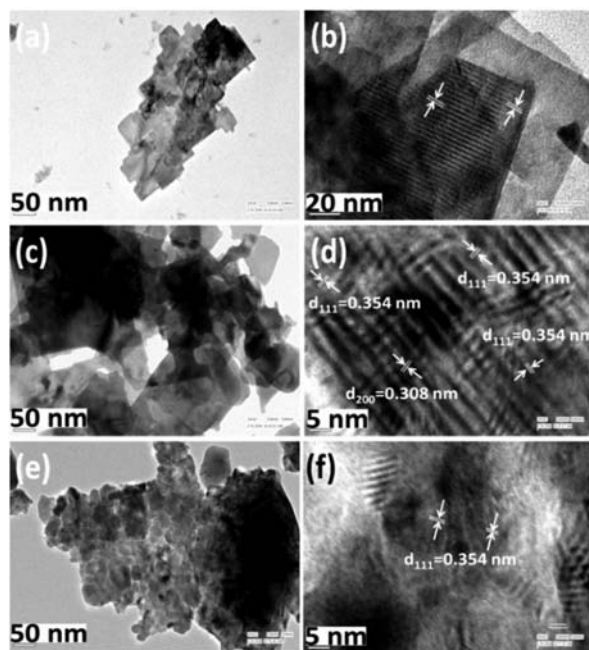


Fig. 5 TEM and HRTEM images of BaF<sub>2</sub>:Ce<sup>3+</sup> (0.1%) nanoparticles: (a and b) as-prepared (60 °C), (c and d) calcined at 400 °C and (e and f) calcined at 600 °C.

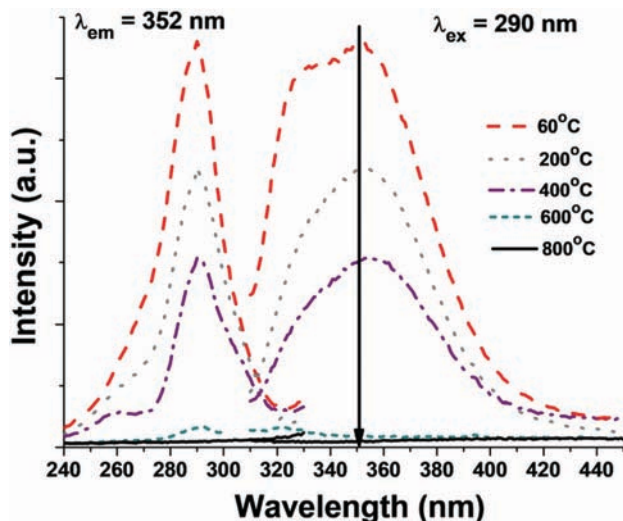


Fig. 6 Photoluminescence excitation and emission spectra of the as-prepared (60 °C) and BaF<sub>2</sub>:Ce<sup>3+</sup> (0.1%) nanoparticles calcined at different temperatures.

for the sample calcined at 600 °C and above (Fig. 6). Obviously, a similar process is observed for the excitation spectra (Fig. 6). These observations suggest that the Ce<sup>3+</sup> emission is suppressed in the samples treated at high calcination temperature. Very recently, we have reported quenching of Eu<sup>3+</sup> emission in BaF<sub>2</sub>:Eu<sup>3+</sup> nanoparticles beyond calcination of 400 °C. A secondary nucleation mediated morphology change was noticed at higher temperature for BaF<sub>2</sub>:Eu<sup>3+</sup> nanoparticles. From elemental mapping, surface area and other analyses, it was concluded that on calcining, Eu<sup>3+</sup> ions are more likely to appear at the surface of the BaF<sub>2</sub> nanoparticles rather than within the asymmetric lattice, which eventually leads to the concentration dependent quenching at higher calcination temperature.<sup>42</sup> It is worth noting that segregation of rare-earth or transition metal ions on the surface of nanoparticles was also documented elsewhere.<sup>44–49</sup> In the present case we also witness a drastic morphology change due to secondary nucleation that is pronounced at higher calcination temperatures. The surface area diminishes to a great extent at higher calcination temperatures (600 and 800 °C), which indicates that Ce<sup>3+</sup> can appear more likely on the surface, which in turn is favorable for concentration quenching. Another reason for the quenching of Ce<sup>3+</sup> emission in the samples with increased calcination temperature is connected with the oxygen atoms (originating from the IL or precursors), which can penetrate the anionic sublattice at high temperature. A similar effect was earlier documented for CaF<sub>2</sub> nanoparticles.

### 3.5 Thermally stimulated luminescence and exoelectron emission

Intrinsic and impurity-related defects are well known to govern the optical and luminescence properties of single and polycrystalline materials, while for nanostructured materials they are expected to become of particular importance. This is connected with the extended grain boundaries and surfaces.

Uncontrolled impurities and defects typically form electron and hole traps which can capture intrinsic electronic excitations and affect the dynamics and efficiency of host-to-impurity energy transfer, which is obviously unwanted for scintillator materials, including BaF<sub>2</sub>:Ce<sup>3+</sup>. To get insight into the nature of traps in optical and luminescence materials a TSL method is widely applied. The method allows determination of the energy level structure and concentration (content) of defects in a particular volume of material and further evaluates their influence on the optical and luminescence properties of the material. Turning to nanostructured materials requires paying greater attention to surface-related defects and therefore applying surface sensitive methods of experimental study such as TSEE. The latter allows the detection of electrons emitted from the sample surface. Thus, simultaneous measurements of TSL and TSEE signals allow identification and sorting of trapping centers into hole and electron ones. Such information is particularly useful when considering the kinetics of processes related to charge transfer from the traps to emission centers.

Fig. 7 presents TSL and TSEE glow curves recorded for the as-prepared (60 °C) and the calcined samples at different temperatures. Obviously, the TSL and TSEE glow curves for all the samples are characterized by a complex structure resulting from a superposition of multiple peaks. The glow curves were fitted assuming first order kinetics of thermal processes.<sup>48,49</sup> The TSEE and TSL activation energies were calculated using specialized software, which is based on widely accepted algorithms and methods.<sup>50,51</sup> The quality of the fittings done in the frame of this research was satisfactory as long as the figure-of-merit (FOM) was normally less than 1%. The kinetics parameters obtained for the TSEE and TSL glow curves, which include the peak maxima ( $T_m$ ), activation energies ( $E_a$ ), and frequency factor ( $S$ ), are gathered in Table 2. On analyzing the glow curves and kinetic parameters such as  $E_a$  and  $S$ , it is noticed that increasing the calcination temperature does not lead to linear variation of the  $E_a$  and  $S$  values. Nevertheless we may highlight the following most pronounced peculiarities of the TSEE and TSL processes in the nanoparticles of 0.1% Ce<sup>3+</sup> doped BaF<sub>2</sub>: first, the as-prepared nanoparticles (P1) demonstrate the presence of relatively deep traps of electron character which appear mostly between 250 and 450 °C (Fig. 7).

Second, the TSL and TSEE glow curves recorded for the nanoparticles calcined at 200 °C (P2) and 400 °C (P3) drastically differ from those demonstrated for the as-prepared sample. This correlates well with the significant changes in the morphology related to the secondary nucleation that occurs in the calcined nanoparticles.

The structure of the defects in the 200 and 400 °C calcined samples is quite similar and is characterized by the presence of traps mostly appearing between 50 and 200 °C. The TSEE output in the corresponding temperature range is very low and is two orders lower than that observed for the as-prepared sample. This suggests that the traps appearing in the nanoparticles calcined at 200 and 400 °C mostly have a hole character (Fig. 7).

Third, the samples calcined at 200 and 400 °C demonstrate the lowest integrated output of TSEE and the highest integrated

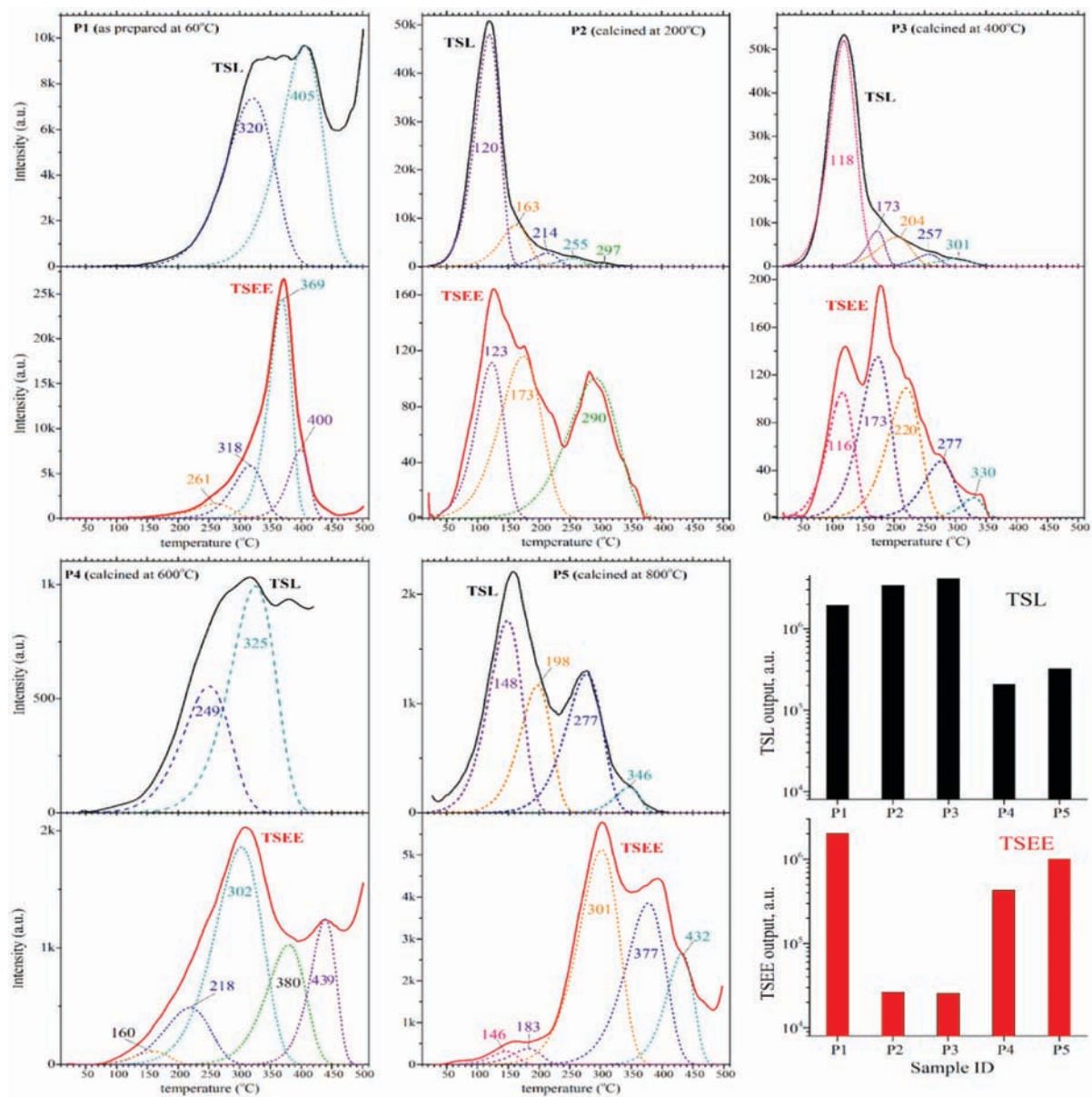


Fig. 7 TSL and TSEE glow curves recorded for the as-prepared (60 °C) (P1) and calcined at 200 °C (P2), 400 °C (P3), 600 °C (P4) and 800 °C (P5) BaF<sub>2</sub>:Ce<sup>3+</sup> (0.1%) nanoparticles exposed to equal doses of the electron beam. Peak maximum temperatures ( $T_m$ , K) are shown near each peak. The bar diagram demonstrates the integrated output of the TSL and TSEE signals as accumulated through the temperature range of the measurement for each sample.

output of TSL. The TSL output is about 100 times higher than that for TSEE in these samples. This suggests that the detected thermal disintegration of trapping centers is mostly related to defects located within the particles' 'volume', not to those related to the surface. This fact correlates with the above described smoothing and blunting of the nanoparticles, which appears as 'healing' of the particle surface, *i.e.* lowering the density of surface-related defects. Note that the most prominent TSL features are followed by the TSEE ones. This fact indicates that the disintegration of trapping centers (defects) is mostly accompanied by the migration of electrons to the glow centers *via* the conduction band. The latter obviously gives rise to electron emission from the nanoparticles. Note that such a phenomenon

becomes less pronounced for the sample calcined at 600 °C (P4) and is not observed for the sample calcined at 800 °C (P5). Finally, turning to the calcination temperature of 600 °C gives rise to a significant (about 20 times) drop of the TSL output in comparison to that observed for the samples calcined at 200 and 400 °C. This is followed by a similar degree increase of the TSEE output. The TSL output further increases by a factor of 1.5 and the TSEE output increases by factor of 2 for the sample calcined at 800 °C. Another important tendency observed for the samples calcined at 600 and 800 °C is related to the domination of deeper electron traps, which appears as a high-temperature shift of the TSEE glow peaks. The most pronounced features in the TSEE and TSL glow curves recorded for the 800 °C calcined sample do not correlate

**Table 2** Kinetic parameters for TSL and TSEE processes in BaF<sub>2</sub>:Ce<sup>3+</sup> (0.1%) nanoparticles irradiated with equal doses of the electron beam

Sample	Process	Kinetic parameter	Peaks				
			1	2	3	4	5
As prepared (60 °C)	TSL	$T_m$	405	320			
		$E_a$	1.12	0.73			
		$S$	$2.17 \times 10^6$	$1.55 \times 10^4$			
	TSEE	$T_m$	400	369	317	261	
		$E_a$	2.34	1.97	1.21	0.82	
		$S$	$7.94 \times 10^{15}$	$6.50 \times 10^{13}$	$3.46 \times 10^8$	$6.57 \times 10^5$	
Calcined at 200 °C	TSL	$T_m$	297	255	214	163	119
		$E_a$	1.39	1.18	1.03	0.69	0.65
		$S$	$4.86 \times 10^{10}$	$4.61 \times 10^9$	$1.20 \times 10^9$	$1.97 \times 10^6$	$4.86 \times 10^6$
	TSEE	$T_m$	290	173	123		
		$E_a$	0.64	0.57	0.48		
		$S$	$6.43 \times 10^3$	$3.30 \times 10^3$	$3.35 \times 10^5$		
Calcined at 400 °C	TSL	$T_m$	301	257	204	173	118
		$E_a$	1.05	1.25	0.72	1.19	0.65
		$S$	$3.19 \times 10^7$	$1.92 \times 10^{10}$	$6.56 \times 10^5$	$9.44 \times 10^{11}$	$6.41 \times 10^6$
	TSEE	$T_m$	330	277	220	173	116
		$E_a$	1.72	1.01	0.76	0.67	0.59
		$S$	$6.74 \times 10^{12}$	$3.62 \times 10^7$	$1.19 \times 10^6$	$8.01 \times 10^5$	$9.95 \times 10^5$
Calcined at 600 °C	TSL	$T_m$	325	249			
		$E_a$	0.79	0.58			
		$S$	$3.76 \times 10^4$	$2.54 \times 10^3$			
	TSEE	$T_m$	439	380	302	218	160
		$E_a$	2.08	1.13	0.70	0.53	0.54
		$S$	$6.81 \times 10^{12}$	$5.03 \times 10^6$	$9.52 \times 10^3$	$1.90 \times 10^3$	$2.03 \times 10^4$
Calcined at 800 °C	TSL	$T_m$	346	277	198	148	
		$E_a$	1.65	0.84	0.73	0.54	
		$S$	$6.89 \times 10^{11}$	$8.35 \times 10^5$	$1.12 \times 10^6$	$5.28 \times 10^4$	
	TSEE	$T_m$	432	377	301	183	146
		$E_a$	1.92	1.10	0.84	0.72	0.70
		$S$	$1.23 \times 10^{12}$	$5.25 \times 10^6$	$3.27 \times 10^5$	$1.86 \times 10^6$	$5.77 \times 10^6$

The notations of the parameters obtained for the TSEE and TSL glow curves are  $T_m$  (peak maxima),  $E_a$  (activation energies) and  $S$  (frequency factor).

with each other and demonstrate most noticeable distinctions. This phenomenon is connected with the formation of new types of defects that do not appear in the smaller nanoparticles synthesized at lower temperatures. Among those defects can be F vacancies (F-centers) that are typical for bulk BaF<sub>2</sub> crystals.<sup>52</sup> This correlates with the formation of larger nanoparticles in high-temperature synthesis (as shown above). Another consequence arising from the formation of larger nanoparticles is connected with the lowering of the surface to volume ratio. This should potentially reduce the interaction of excited Ce<sup>3+</sup> ions with the surface-related defects. It is worth noting that the appearance of the TSL glow curve recorded for the nanoparticles calcined at 800 °C well correlates with that recently documented for an optimized BaF<sub>2</sub>:Ce<sup>3+</sup> nanophosphor with an average particle size of 100 nm.<sup>53</sup>

Fig. 8 shows an energy level diagram for the data presented in Table 2. The diagram depicts the Ce<sup>3+</sup> 4f ground state and the lowest energy 5d state located within the forbidden gap.<sup>54</sup> The energy levels of the electron and hole traps are located through the above-described synchronic measurements of TSL and TSEE glow curves. The diagram demonstrates the fact that the most effective mechanism to transfer energy from host electronic excitations to Ce<sup>3+</sup> ions at high temperatures is realized through the electron-hole recombination process.<sup>55</sup>

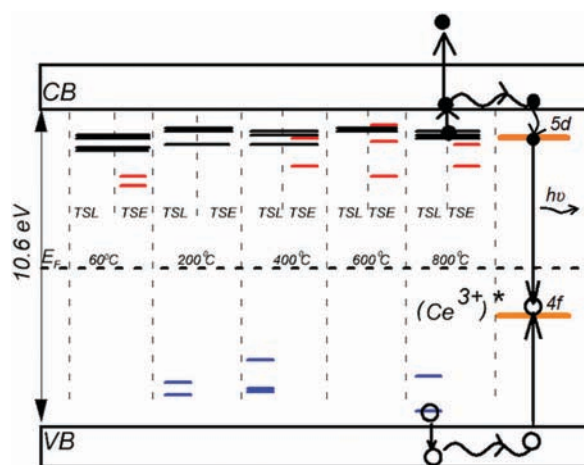


**Fig. 8** Energy level diagram demonstrating the location of electron and hole traps in BaF<sub>2</sub>:Ce<sup>3+</sup> (0.1%) nanoparticles calcined at different temperatures. Black-marked energy levels correspond to the traps which are simultaneously detected through TSEE and TSL. Red- and blue-marked energy levels correspond to the traps detected only through TSEE or TSL, respectively.

Thermal activation of electron and hole traps results in delocalization of the carriers to the conduction and valence

bands. The delocalized carriers may further interact with cerium ions. Excitation of a  $\text{Ce}^{3+}$  ion generally starts with the capture of a hole from the VB and formation of a  $\text{Ce}^{4+}$  ion, which further attracts an electron from the CB to promote recombination. The dynamics of this process can be significantly affected by re-trapping of carriers on defects.

It is worth noting that the TSL and TSEE techniques have obvious limitations. First of all, there is some degree of uncertainty in the actual temperature of the sample. The temperature gradient between the lower and upper surface of the sample may vary depending on the crystal structure and density of the sample. Structural inhomogeneity may lead to the appearance of additional glow peaks. It is quite often that the TSL curves recorded for single crystals differ from those recorded for polycrystalline or powdered samples.<sup>56</sup> Another phenomenon that may give rise to uncertainty in the interpretation of TSEE features arises from thermal decomposition of the organic precursor or ionic liquid remaining on the surface of the nanoparticles. To exclude the uncertainties mentioned above, additional studies with VUV and EPR spectroscopy are required to get insight into the molecular and energy structure of the defects observed.

## 4. Conclusion

In summary, we have successfully synthesized single phase  $\text{BaF}_2$  nanoparticles doped with 0.1%  $\text{Ce}^{3+}$  using a task specific ionic liquid ( $[\text{C}_4\text{mim}][\text{BF}_4]$ ) where the IL works as a solvent, a templating agent and a fluoride source, *i.e.* all 'three in one'. On calcining the samples from 60 to 800 °C, a significant effect on the lattice strain and morphology is observed. The lattice strain changes from tensile to compressive on increasing the calcination temperature. However, the morphology of the nanoparticles changes from a cubic/rectangular shape (as-prepared) to layer like structures (calcining the samples above 600 °C). This morphological change is fundamentally controlled by secondary nucleation of nanoparticles at high temperature (>600 °C). Another important effect of the calcination temperature is found on the PL intensity of the nanoparticles, in which the emission intensity is abruptly decreased with increasing the calcination temperature and vanishes for the sample calcined at 600 °C. Simultaneous measurements of TSL and TSEE glow curves allowed general identification of hole and electron trapping centers, which were found to significantly vary in the samples calcined at different temperatures. Analysis reveals that along with deeper electron traps that appear as a high-temperature shift of the TSEE glow peaks for both 600 and 800 °C, some new types of defects like F vacancies (F-centres) can be present and affect the luminescence at high calcination temperature. The samples prepared at high calcination temperature are also shown to experience quenching of luminescence related to segregation of  $\text{Ce}^{3+}$  dopant ions on the nanoparticles' surface as a result of secondary nucleation mediated morphology changes at higher calcination temperature. All these phenomena cumulatively quench the  $\text{Ce}^{3+}$  luminescence in nanoparticles calcined at

high temperature. Nevertheless, the presented results suggest the presence of an evidently strong correlation between the synthesis conditions and morphology, defect structure and luminescence characteristic of nanoparticles that can be further used for tailoring nanomaterials with controlled properties.

## Conflicts of interest

There are no conflicts to declare.

## Acknowledgements

The authors would like to acknowledge financial support from the Science and Engineering Research Board (SERB) [SERB No: SB/FT/CS-014/2014], and Board of Research in Nuclear Sciences (BRNS) [Sanction No. 34/14/27/2016-BRNS/34368], Government of India. P. G. acknowledges SERB for providing an International Travel Grant (ITS/2018/003736) to participate in a conference in Russia. The authors acknowledge the Sophisticated Instrumentation Centre (SIC) for SEM, Department of Chemistry for PXRD analysis and PURSE programme sanctioned by the Department of Science and Technology (DST), Govt of India. The authors also acknowledge AIIMS New Delhi for TEM characterization. A. I. S., K. V. I. and I. I. L. acknowledge partial support from the UrFU Competitiveness Enhancement Program.

## References

- 1 X. Qin, X. Liu, W. Huang, M. Bettinelli and X. Liu, *Chem. Rev.*, 2017, **117**, 4488–4527.
- 2 S. Gai, C. Li, P. Yang and J. Lin, *Chem. Rev.*, 2014, **114**, 2343–2389.
- 3 S. V. Eliseeva and J.-C. G. Bünzli, *Chem. Soc. Rev.*, 2010, **39**, 189–227.
- 4 R. K. Sharma, A.-V. Mudring and P. Ghosh, *J. Lumin.*, 2017, **189**, 44–63.
- 5 C. D. S. Brites, P. P. Lima, N. J. O. Silva, A. Millán, V. S. Amaral, F. Palacio and L. D. Carlos, *New J. Chem.*, 2011, **35**, 1177–1183.
- 6 X.-C. Shao, S.-M. Zhou, Y.-R. Tang, X.-Z. Yi, D.-M. Hao and J. Chen, *J. Inorg. Mater.*, 2018, **33**, 1119–1123.
- 7 M. Šimurda, M. Boča, P. Švec, P. Švec Jr., D. Janičkovič, Z. N. Shiand and J. Mlynáriková, *New J. Chem.*, 2018, **42**, 4612–4623.
- 8 N. P. Singh, N. Kumam, L. P. Singh, N. R. Singh and K. Srivastava, *New J. Chem.*, 2019, **43**, 1328–1339.
- 9 D. Valiev, T. Han, S. Stepanov, V. Vaganov and V. Paygin, *Mater. Res. Express*, 2018, **5**, 096201.
- 10 T. Kato, G. Okada, K. Fukuda and T. Yanagida, *Radiat. Meas.*, 2017, **106**, 140–145.
- 11 M. Siebold, S. Bock, U. Schramm, B. Xu, J. L. Doualan, P. Camy and R. Moncorgé, *Appl. Phys. B: Lasers Opt.*, 2009, **97**, 327–338.
- 12 V. V. Vistovskyy, A. V. Zhyshkovich, O. O. Halyatkin, N. E. Mitina, A. S. Zaichenko, P. A. Rodnyi, A. N. Vasil'ev,

- A. V. Gektin and A. S. Voloshinovskii, *J. Appl. Phys.*, 2014, **116**, 054308.
- 13 E. A. McKigney, R. E. Del Sesto, L. G. Jacobsohn, P. A. Santi, R. E. Muenchausen, K. C. Ott, T. M. McCleskey, B. L. Bennett, J. F. Smith and D. W. Cooke, *Nucl. Instrum. Methods Phys. Res., Sect. B*, 2007, **579**, 15–18.
- 14 R. K. Feller, G. M. Purdy, D. Ortiz-Acosta, S. Stange, A. Li, E. A. McKigney, E. I. Esch, R. E. Muenchausen, R. Gilbertson, M. Bacrania, B. L. Bennett, K. C. Ott, L. Brown, C. S. Macomber, B. L. Scott and R. E. Del Sesto, *J. Mater. Chem.*, 2011, **21**, 5716–5722.
- 15 L. G. Jacobsohn, K. B. Sprinkle, C. J. Kucera, T. L. James, S. A. Roberts, H. Qian, E. G. Yukihara, T. A. DeVol and J. Ballato, *Opt. Mater.*, 2010, **33**, 136–140.
- 16 X. Duan, J. Ma, J. Lianc and W. Zheng, *CrystEngComm*, 2014, **16**, 2550–2559.
- 17 P. Ghosh, R. K. Sharma, Y. N. Chouryal and A.-V. Mudring, *RSC Adv.*, 2017, **7**, 33467–33476.
- 18 R. K. Sharma, Y. N. Chouryal, S. Chaudhari, J. Saravanakumar, S. R. Dey and P. Ghosh, *ACS Appl. Mater. Interfaces*, 2017, **9**, 11651–11661.
- 19 S. Anghel, S. Golbert, A. Meijerink and A.-V. Mudring, *J. Lumin.*, 2017, **189**, 2–8.
- 20 J. Cybińska, C. Lorbeer and A.-V. Mudring, *J. Mater. Chem.*, 2012, **22**, 9505–9508.
- 21 C. Lorbeer, F. Behrends, J. Cybinska, H. Eckert and A.-V. Mudring, *J. Mater. Chem. C*, 2014, **2**, 9439–9450.
- 22 R. D. Rogers and K. R. Seddon, *Science*, 2003, **302**, 792–793.
- 23 M. Armand, F. Endres, D. R. Macfarlane, H. Ohno and B. Scrosati, *Nat. Mater.*, 2009, **8**, 621–629.
- 24 J. P. Hallett and T. Welton, *Chem. Rev.*, 2011, **111**, 3508–3576.
- 25 S. Zhang, J. Sun, X. Zhang, J. Xin, Q. Miao and J. Wang, *Chem. Soc. Rev.*, 2014, **43**, 7838–7869.
- 26 P. Ghosh and A.-V. Mudring, *Nanoscale*, 2016, **8**, 8160–8169.
- 27 A. Meijerink, W. J. Schipper and G. Blasse, *J. Phys. D: Appl. Phys.*, 1991, **24**, 997–1002.
- 28 P. L. Antonio and L. V. E. Caldas, *Radiat. Meas.*, 2017, **106**, 538–542.
- 29 N. Kunkel, A. D. Sontakke, S. Kohaut, B. Vianaand and P. Dorenbos, *J. Phys. Chem. C*, 2016, **120**, 29414–29422.
- 30 M. Buryi, P. Bohacek, K. Chernenko, A. Krasnikov, V. V. Laguta, E. Mihokova, M. Nikl and S. Zazubovich, *Phys. Status Solidi B*, 2016, **253**, 895–910.
- 31 V. Y. Degoda, Y. P. Kogut, I. M. Moroz and F. A. Danevich, *J. Lumin.*, 2017, **183**, 424–432.
- 32 D. O. Junot, M. A. C. dos Santos, P. L. Antonio, L. V. E. Caldas and D. N. Souza, *Radiat. Meas.*, 2014, **71**, 99–103.
- 33 M. E. Haghiri, E. Saion, N. Soltani, W. S. wan Abdullah, M. Navasery, K. R. E. Saraee and N. Deyhimi, *J. Alloys Compd.*, 2014, **582**, 392–397.
- 34 O. T. Antonyak, V. V. Vistovskyy, A. V. Zhyshkovych and I. M. Kravchuk, *J. Lumin.*, 2015, **167**, 249–253.
- 35 R. Hemam, L. R. Singh, S. D. Singh and R. N. Sharan, *J. Lumin.*, 2018, **197**, 399–405.
- 36 M. Kumar and S. K. Gupta, *J. Lumin.*, 2015, **168**, 151–157.
- 37 B. Zhou, L. Tao, Y. H. Tsang and W. Jin, *J. Mater. Chem. C*, 2013, **1**, 4313–4318.
- 38 F. Vetrone, R. Naccache, V. Mahalingam, C. G. Morgan and J. A. Capobianco, *Adv. Funct. Mater.*, 2009, **19**, 2924–2929.
- 39 A. S. S. Shafiqah, Y. M. Amin, R. M. Nor and D. A. Bradley, *Radiat. Phys. Chem.*, 2015, **117**, 102–107.
- 40 K. F. Peters, Y.-W. Chung and J. B. Cohen, *Appl. Phys. Lett.*, 1997, **71**, 2391–2393.
- 41 K. Dick, T. Dhanasekaran, Z. Zhang and D. Meisel, *J. Am. Chem. Soc.*, 2002, **124**, 2312–2317.
- 42 R. K. Sharma, S. Nigam, Y. N. Chouryal, S. Nema, S. P. Bera, Y. Bhargava and P. Ghosh, *ACS Appl. Nano Mater.*, 2019, **2**, 927–936.
- 43 R. Visser, P. Dorenbos, C. W. E. van Eijk, A. Meijerink, G. Blassé and H. W. den Hartog, *J. Phys.: Condens. Matter*, 1993, **5**, 1659–1680.
- 44 J. Bang, H. Yang and P. H. Holloway, *Nanotechnology*, 2006, **17**, 973.
- 45 S.-J. Shih, Y.-Y. Wu and K. B. Borisenko, *J. Nanopart. Res.*, 2011, **13**, 7021–7028.
- 46 X. Weng, B. Perston, X. Z. Wang, I. Abrahams, T. Lin, S. Yang, J. R. G. Evans, D. J. Morgan, A. F. Carley, M. Bowker, J. C. Knowles, I. Rehman and J. A. Darr, *Appl. Catal., B*, 2009, **90**, 405–415.
- 47 N. Salah, N. D. Alharbi, S. S. Habib and S. P. Lochab, *J. Nanomater.*, 2015, **2015**, 1–7, DOI: 10.1155/2015/136402.
- 48 R. Chen, *J. Appl. Phys.*, 1969, **40**, 570–585.
- 49 A. J. J. Bos, *Radiat. Meas.*, 2007, **41**, S45–S56.
- 50 A. I. Slesarev, *Bull. Ural State Tech. Univ.*, 2006, **5**, 174–179.
- 51 K. S. Chung, H. S. Choe, J. I. Lee, J. L. Kim and S. Y. Chang, *Radiat. Prot. Dosim.*, 2005, **115**, 345–349.
- 52 A. J. Wojtowicz, P. Szupryczynski, J. Glodo, W. Drozdowski and D. Wisniewski, *J. Phys.: Condens. Matter*, 2000, **12**, 4097–4124.
- 53 K. H. Gavhane, M. S. Bhadane, A. P. Jadhav, B. J. Patil, V. N. Bhoraskar, S. S. Dahiwalé and S. D. Dhole, *J. Lumin.*, 2019, **209**, 316–320.
- 54 P. A. Rodnyi, I. V. Khodyuk and G. B. Stryganyuk, *Phys. Solid State*, 2008, **50**, 1639–1643.
- 55 E. A. Radzhabov and A. I. Nepomnyashchikh, *Russ. Phys. J.*, 2000, **43**, 205–210.
- 56 T. Yanagid, Y. Fujimoto, Y. Yokot, K. Kamad, S. Yanagid, A. Yoshikaw, H. Yagi and T. Yanagitani, *Radiat. Meas.*, 2011, **46**, 1503–1505.

## Supporting Information

### A closer look at defects and luminescence of nanocrystalline fluorides synthesized via ionic liquids: the case of Ce<sup>3+</sup>-doped BaF<sub>2</sub>

Rahul Kumar Sharma,<sup>a</sup> Yogendra Nath Chouryal,<sup>a</sup> Anatoly I. Slesarev,<sup>b</sup> Konstantin V. Ivanovskikh,<sup>\*b</sup> Ivan I. Leonidov,<sup>c,d</sup> Sandeep Nigam<sup>e</sup> and Pushpal Ghosh<sup>\* a</sup>

<sup>a</sup>School of Chemical Sciences and Technology, Department of Chemistry, Dr. H. S. Gour University (A Central University), Sagar-470003, Madhya Pradesh, India. [Email-pushpalghosh27@gmail.com](mailto:pushpalghosh27@gmail.com).

<sup>b</sup>Institute of Physics and Technology, Ural Federal University, 620002, Ekatarinburg, Russia,

<sup>c</sup>School of Engineering, Ural Federal University, 620002, Ekaterinburg, Russia

<sup>d</sup>Institute of High-Temperature Electrochemistry, UB RAS, 620137, Ekaterinburg, Russia

<sup>e</sup>Chemistry Division, Bhabha Atomic Research Centre, Trombay, Mumbai-400085, India

---

**Chemicals:** Barium Acetate Ba(CH<sub>3</sub>COO)<sub>2</sub> (Himedia), Cerium Nitrate (Ce(NO<sub>3</sub>)<sub>3</sub>·6H<sub>2</sub>O) (Alfa Aesar), Dichloromethane (CH<sub>2</sub>Cl<sub>2</sub>), Deionised (DI) water from CDH (Central Drug House), 1-methylimidazole (C<sub>4</sub>H<sub>6</sub>N<sub>2</sub>) (Alfa Aesar), n-Butyl Bromide (C<sub>4</sub>H<sub>9</sub>Br), Sodium Tetrafluoroborate (NaBF<sub>4</sub>), Acetone (C<sub>3</sub>H<sub>6</sub>O), Charcoal from Loba Chemie, Acetonitrile, Ethanol (C<sub>2</sub>H<sub>5</sub>OH) from Merck.

**Synthesis of [C<sub>4</sub>mim][Br] ionic liquid:** Modifying a literature procedure, 12.37 ml of n-butyl bromide (0.166 mol, Himedia) and 10 ml of N-methyl imidazole (0.126 mol, Alfa Aesar) are stirred under argon (Ar) gas atmosphere at room temperature (RT) for 72 hours in a 250 ml round bottom flask in order to get complete reaction. As a result, solid white crystals were obtained. Ethyl acetate was added to the raw product and crushed it to fine crystals. After that the resultant crude product was washed twice with ethyl acetate and again re-crystallized with acetonitrile. The obtained product was dried in vacuum at 25°C for 24 hours to get white solid product.<sup>1</sup>

**Synthesis of [C<sub>4</sub>mim][BF<sub>4</sub>] ionic liquid:** The room temperature ionic liquid (RTIL) [C<sub>4</sub>mim][BF<sub>4</sub>] was prepared by adding NaBF<sub>4</sub> (21 gm) and 1-butyl-3-methylimidazolium bromide [C<sub>4</sub>mim][Br] (42 gm) in acetone (100 ml) and allowed for stirring at RT for 3-4 days.<sup>2-3</sup> The obtained product was filtered and then kept for stirring for further 16 hours with 1 gm activated charcoal. The activated charcoal was filtered and acetone was finally removed

by rotary evaporator in vacuum. The obtained product was further mixed with about 60 ml of dichloromethane (at least 3-4 times) to make it free of impurities. A little amount of silver nitrate solution was added to the washed ionic liquid to confirm the chloride ions. The pale yellowish liquid was isolated and further dried in a vacuum for 12 hours.

### Williamson and Hall method

The lattice strain can be calculated by using Williamson and Hall method:<sup>4</sup>

$$\frac{\beta \cos \theta}{\lambda} = \frac{1}{D} + \eta \frac{\sin \theta}{\lambda} \quad (1)$$

When  $\beta \cos \theta / \lambda$  vs  $\sin \theta / \lambda$  is plotted, lattice strain ( $\eta$ ) can be quantitatively determined from the slope of the graph and crystallite size from the intercept.

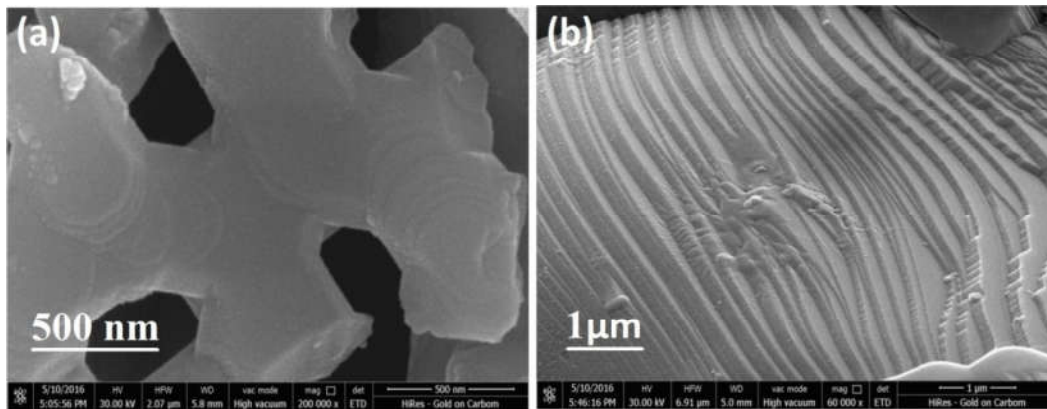


**Figure S1.** FESEM images of  $\text{BaF}_2:\text{Ce}^{3+}(0.1\%)$  nanoparticles calcined at  $600^\circ\text{C}$  (a) and  $800^\circ\text{C}$  (b).

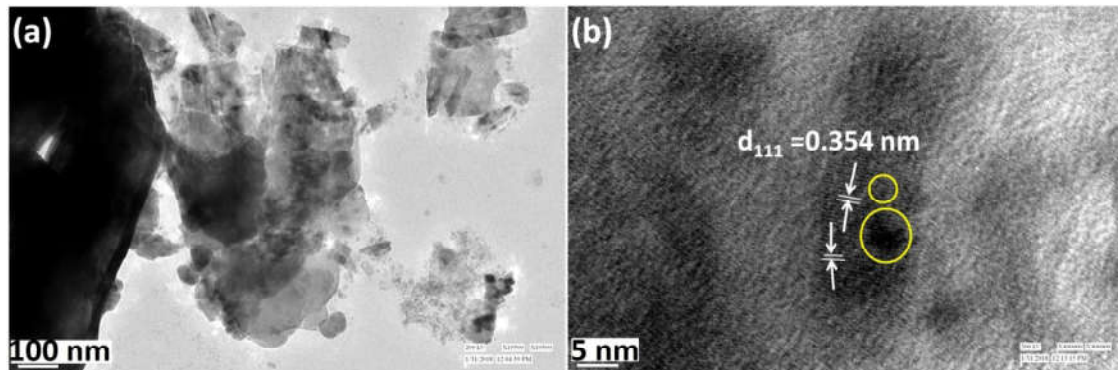


**Figure S2.** TEM and HRTEM images of  $\text{BaF}_2:\text{Ce}^{3+}(0.1\%)$  nanoparticles calcined at  $800^\circ\text{C}$ .

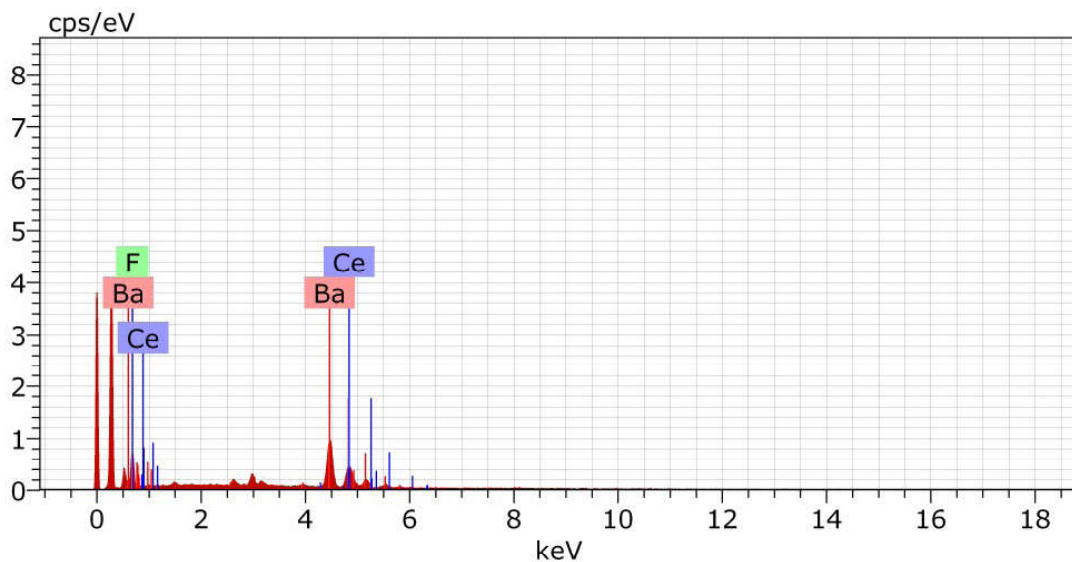


**Figure S3.** EDX spectrum of as-prepared BaF<sub>2</sub>:Ce<sup>3+</sup> (0.1%) nanoparticles (P1).

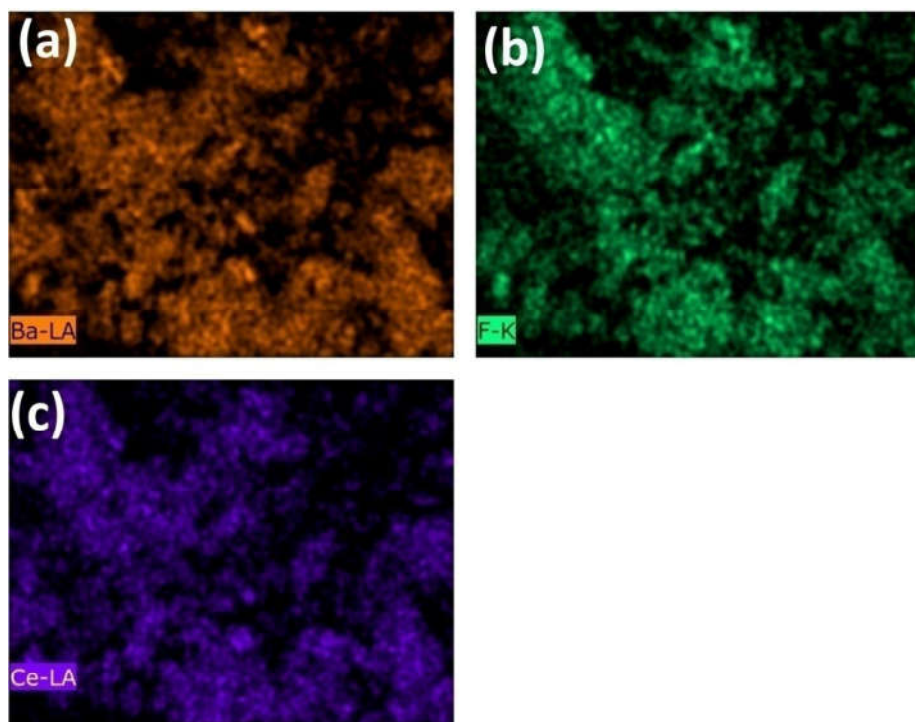


**Figure S4.** Elemental mapping (a-c) of as-prepared BaF<sub>2</sub>:Ce<sup>3+</sup> (0.1%) nanoparticles (P1).

**Reference:**

1. R. K. Sharma, Y. N. Chouryal, S. Chaudhari, J. Saravanakumar, S. R. Dey and P. Ghosh, *ACS Appl. Mater. Interfaces*, 2017, **9**, 11651–11661.

2. S. Anghel, S. Golbert, A. Meijerink , A.-V. Mudring, *J. Lumin.*, 2017,**189**, 2–8.
3. C. Lorbeer, F. Behrends, J. Cybinska, H. Eckert and A.-V. Mudring, *J. Mater. Chem. C*, 2014, **2**, 9439–9450.
4. R. K. Sharma, S. Nigam, Y. N. Chouryal, S. Nema, S. P. Bera, Y. Bhargava and P. Ghosh, *ACS Appl. Nano Mater.*, 2019, **2**, 927-936.